

First Thomson scattering results from AWAKE's helicon plasma source

C Stollberg^{1,*} , Ph Guittienne¹ , R Karimov¹ , A Sublet² , I Furno¹ , B Vincent¹ ,
Y Andrebe¹ and B Buttenschön³ 

¹ Ecole Polytechnique Fédérale de Lausanne (EPFL), Swiss Plasma Center (SPC), CH-1015 Lausanne, Switzerland

² CERN, 1211 Geneva 23, Switzerland

³ Max Planck Institute for Plasma Physics, Wendelsteinstr. 1, D-17491 Greifswald, Germany

E-mail: christine.stollberg@epfl.ch

Received 1 July 2024, revised 22 August 2024

Accepted for publication 19 September 2024

Published 30 September 2024



Abstract

We present the first results of electron density and temperature measurements obtained from Thomson scattering at the helicon plasma source (HPS) for the AWAKE project. These measurements are compared to simulation results from a 1D power and particle balance model (PPM), confirming that the plasma can be fully sustained by collisional power dissipation. The variations in plasma parameters under different experimental conditions are evaluated in the PPM framework. We discuss current limitations of the model and propose possible improvements. Additionally, we suggest modifications to the existing HPS setup to enhance axial plasma homogeneity.

Keywords: AWAKE, plasma wakefield acceleration, helicon plasma source, Thomson scattering, particle and power balance

1. Introduction

Plasma wakefield acceleration [1, 2] is an attractive scheme where electrons are captured in a plasma wave and accelerated by the wave's electric field. Electron energies in the GeV range can be achieved in university scale experiments, using high-intensity lasers to drive the plasma wave [3]. Even higher energies can be achieved when the plasma wave is excited by an energetic proton bunch. This is the principle underlying the AWAKE (Advanced WAKEfield Experiment) collaboration at CERN which demonstrated the acceleration of electrons to 2 GeV over an acceleration length of 10 m [4]. The next challenge is to prove the scalability of the achieved electron energy gain with the accelerator length. In AWAKE run 2c and run

2d [5], two plasma sources will be used: (i) a self-modulator where the 400 GeV proton bunch of 230 ps length and 200 μm transverse radius undergoes self-modulation, which results in proton bunchlets with a modulation frequency of the electron plasma frequency f_{pe} , and (ii) a 10 m *accelerator* where the proton bunchlets drive the plasma wake that will accelerate the witness electron bunch, subsequently, to multi GeVs. For experiments following run 2, an accelerator with a length well beyond 10 m is required to access electron energies relevant for particle physics experiments [5].

The requirements for the AWAKE plasma accelerator are extremely challenging: (i) An electron density of $7 \times 10^{20} \text{ m}^{-3}$ was defined as the nominal AWAKE density to reach accelerating gradients in the order of 1 GV/m while promoting efficient self-modulation of the initial proton bunch that is focused to a transverse radius of 200 μm [6, 7]. (ii) The relative variation of the electron density along the entire length of the plasma has to be below 0.25% in order to guarantee that the accelerated electron bunch remains in phase with the wakefields. For the *self-modulator*, the constraint on homogeneity is less rigorous, but the possibility to introduce a well controlled density

* Author to whom any correspondence should be addressed.



Original Content from this work may be used under the terms of the [Creative Commons Attribution 4.0 licence](https://creativecommons.org/licenses/by/4.0/). Any further distribution of this work must maintain attribution to the author(s) and the title of the work, journal citation and DOI.

gradient or density step is desirable to enhance the accelerating wake field amplitude [8]. (iii) The plasma source has to be scalable in length, well beyond 10 m, and compatible with the rough environment of the tunnel of the CERN accelerator that provides the initial proton and witness electron bunches.

During AWAKE run 1 [4], a single 10 m-long rubidium vapor source was utilized as combined *self-modulator* and *accelerator* [9, 10]. Careful control of the temperature and base pressure along the source generated homogenous plasmas or smooth density gradients. Currently, the rubidium source is upgraded to produce a density step and its effect on the self-modulation of the proton bunch will be tested, shortly. However, as the plasma is generated by laser ionization, the rubidium source can not be scaled to much more than 10 m.

Recently, a 10-m discharge plasma source (DPS) [11] has been developed and tested very successfully in the AWAKE experiment at CERN for its potential application as *self-modulator*. The relatively simple design comprises two electrodes, a cathode at one extremity and an anode at the other, that are driven by a fast ignition voltage pulse and a slower heater current pulse. The DPS demonstrated compatibility with the tunnel environment and integration into the CERN facilities, great flexibility in the plasma parameters (electron density and ion mass by using different gas species), ease of use, and reproducibility. During the campaign, the effects of the plasma parameters on the self modulation of a proton bunch and various diagnostics were extensively tested [12–14]. However, the uniformity of the electron density, the key-requirement for the future scalable *accelerator*, was not yet assessed.

Also under consideration as plasma source for AWAKE is the helicon plasma source (HPS), which is based on radio-frequency (RF) antennas, and, therefore, intrinsically scalable in length. Helicon plasma sources are known for their capability to produce relatively high density plasmas at relatively low input power [15]. However, the densities required for AWAKE are well beyond the usual operating regime of pulsed helicon sources. Few systems for high-power helicon sources are currently under development. The applications involve several fusion-related subjects such as plasma-wall interaction at MPEX [16, 17], current drive at DIII-D [18] and negative-ion production for neutral beams at RAID [19, 20]. Furthermore, the Variable Specific Impulse Magnetoplasma Rocket (VASIMR) project [21] is exploring the potential of helicon sources for plasma propulsion and the high power helicon (HPH) device [22] is developed to investigate the physics of the solar wind. Helicon source development related to AWAKE also takes place with the magnetized anisotropic ion apparatus (MARIA) [23, 24] and the Madison AWAKE Prototype (MAP) [25, 26] at the University of Wisconsin, Madison. The laboratory focuses on basic helicon science to contribute to HPS design considerations, and diagnostics development. Most of these helicon sources use an input power of few 10 to 100 kW and generate densities in the range of several 10^{-19} m^{-3} up to $1 \times 10^{-20} \text{ m}^{-3}$, almost one order of magnitude below the required density for AWAKE.

The AWAKE plasma source development program also seeks to design a diagnostic suitable to be implemented in the tunnel as a monitor for shot-to-shot stability and axial electron density homogeneity and that can provide a sensitivity of 0.25%. This development is especially challenging, as some criteria seem mutually exclusive. Electrical probes can not be used in the AWAKE plasma sources due to the small radial scale of the plasma devices and the perturbative character of the probes. Interferometry and optical emission spectroscopy (OES) can be potentially used as real-time monitor. However, the inherent integration over the line of sight and the need for reconstruction algorithms compromise the required locality and sensitivity of the measurement. Local diagnostics based on active spectroscopy, such as Thomson scattering (TS) [27] or laser induced fluorescence (LIF) [24], have to overcome relatively low signal levels in the AWAKE density regime so that data has to be acquired over many plasma cycles. Furthermore, those techniques require an absolute calibration, which imposes additional uncertainties on the absolute electron densities. Other techniques, such as micro wave cut-off diagnostics, are under development.

Here, we report the first results of a TS diagnostics that was newly implemented on the HPS at CERN. The TS setup provides a local and time resolved measurement of the electron density and temperature in the center of the plasma source for a variety of initial conditions. The measurement results are compared to detailed 1D simulation results of the plasma, which provide guidance for the planning of a future modular design for a 2.5 m-long helicon prototype.

The present paper is structured as follows: in section 2 we will present the technical details of the HPS and the TS diagnostic setup, followed by the results in section 3. We then introduce the plasma model in section 4 and interpret the experimental results based on the simulation results. In section 6 we discuss our findings and future work and we close with a conclusion in section 7.

2. Experimental setup

2.1. The AWAKE HPS

The helicon plasma source (HPS) for AWAKE was originally developed at the Max Planck institute for Plasma Physics (IPP) in Greifswald, Germany, and characterized with a CO_2 interferometer, as reported in [28]. After demonstrating the nominal AWAKE density of $7 \times 10^{-20} \text{ m}^{-3}$, the system was reinstalled at CERN with some improvements. We will shortly describe the plasma source itself, the changes implemented at CERN and the operating parameters anticipated to generate highest densities as found in [28].

The plasma is generated in a 1 m long quartz tube with 44 mm inner diameter, equipped with three optical view ports, as shown in figure 1. The axial magnetic field B_0 of up to 125 mT is provided by a DC current of $\leq 400 \text{ A}$ through five water-cooled copper coils. Three RF antennas are equidistantly (230 mm) distributed along the quartz tube and

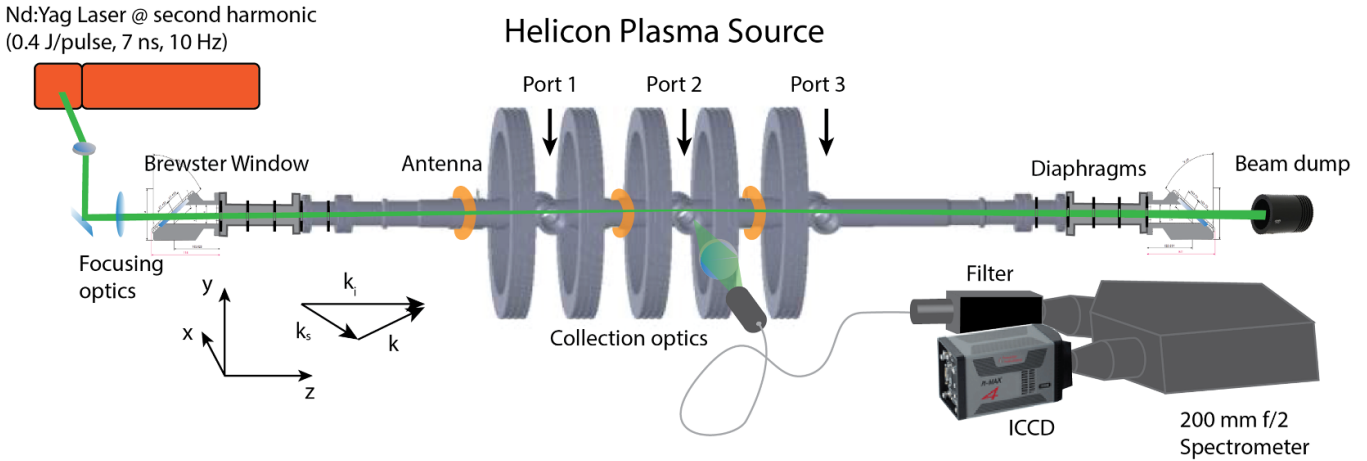


Figure 1. Outline of the experimental setup.

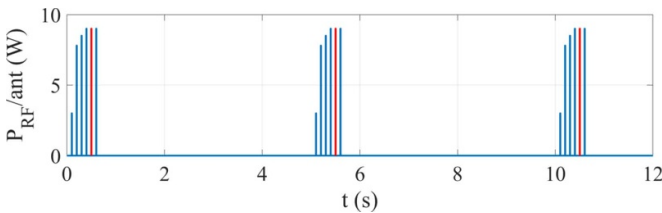


Figure 2. Illustration of the RF sequence used at the HPS for $P_{\text{RF}} = 9 \text{ kW/ant}$. Each RF pulse is 5 ms long. The measurement is obtained at the 5th pulse (marked in red). The RF sequence is repeated every 5 s.

over the view ports and fed by three individual RF power supplies delivering $P_{\text{RF}} \leq 12 \text{ kW}$ per antenna.

The RF generators are operated at $f_{\text{RF}} = 13.56 \text{ MHz}$. They are run in a ramp-up sequence with six individual pulses, the last three reaching the nominal power. The pulses are generated at a frequency of 10 Hz with a fast ($2 \mu\text{s}$) rise time and a pulse duration of 5 ms, each. Due to the long separation (100 ms) between the single RF pulses, the plasma generated in each pulse can be regarded as independent of the other pulses. The ramp-up sequence was necessary only due to technical constraints of the RF generators. To limit the heat load on the antennas and the vacuum chamber, the RF sequence is repeated every 5 s, resulting in an effective operation frequency of 0.2 Hz, as illustrated in figure 2. Each RF generator is coupled to its antenna by a manual floating L-type capacitive matching circuit to minimize reflected power. The matching is adjusted to the steady-state plasma conditions. Each time the experimental parameters (in particular DC magnetic field and RF power) are changed, the matching is adjusted accordingly. The relative phase of the RF field provided to the three antennas can be controlled at the RF power supplies that are operated with the same master clock. Note that the phase relation between the antennas can strongly affect the matching network and the achieved plasma parameters.

During reinstallation of the HPS at CERN several experimental details were altered compared to the previous

setup operated at IPP Greifswald. In the initial setup [28], 75-mm-long half-helical antennas generating $m = 1$ modes were employed. With this setup, no resonant effects were observed. In particular, the electron density that is expected to dominantly propagate a helicon wave at the same wavelength as the half-helical antenna, was not generated preferentially. Consequently, we have opted to replace the original antennas with $m = 0$ mode ring antennas that provide several advantages. (i) The 10-mm-wide copper rings can be easily fabricated and installed on the HPS. (ii) The $m = 0$ mode promotes symmetric plasma generation in both, the upstream and downstream directions. (iii) The cross-talk between antennas, where one receives the RF field generated by the others, is reduced due to a smaller effective surface area and the larger effective inter-antenna distance. Furthermore, the pumping scheme of the HPS was changed from pumping and gas feed being situated at opposite sides of the quartz tube (steady-state flow) to a scheme where they are installed on the same side (resulting in an almost stationary gas situation). The previously employed pump was exchanged by a turbo molecular pump and a scroll pump to achieve a lower base pressure. Additionally, adaptation to the CERN laboratory required the modification of the grounding scheme of the HPS, as well as utilization of longer RF cables and different positions of DC ceramic breakers at the ends of the vacuum chamber.

The HPS is operated with argon due to its relatively low ionization energy of 15.76 eV, its inert chemical character and its good availability. The pressure is adjusted to a few (5 – 10) Pa, typically, such that the nominal AWAKE density can be achieved at an ionization degree of 0.25 – 0.5. Furthermore, a simple power and particle balance model (PPM) [29] showed that with a power of $\approx 30 \text{ kW}$ the required density can be achieved with $T_e < 2 \text{ eV}$. Indeed, in [28], the nominal AWAKE density of $7 \times 10^{-20} \text{ m}^{-3}$ was achieved for $P_{\text{RF}} = 27 \text{ kW}$, delivered by three antennas (9 kW/antenna), at $p = 8 \text{ Pa}$ and $B_0 = 106 \text{ mT}$. The RF phase between the single antennas was adjusted at the RF source to be 180:270:0 for antennas 1:2:3.

2.2. The TS system

A new TS diagnostics was installed to measure the local electron density n_e and temperature T_e , and to benchmark the HPS operation after reinstallation at CERN. The TS system was developed on the Resonant Antenna Ion Device (RAID) [19] at EPFL as improvement of a previous diagnostics [27]. Using the second harmonic of the Nd:YAG laser allowed us to replace the polychromator and avalanche photo diodes by a spectrometer and a gated ICCD camera, as demonstrated in [30]. Furthermore, the shorter wavelength guarantees that the diagnostic is operating in the incoherent TS regime for the expected HPS densities. The setup is described in detail in the following.

The TS setup relies on the second harmonic of a Quantel Brilliant B,Q -switched Nd:YAG laser with an energy of 350 mJ/pulse at 532 nm. The laser operates at 10 Hz with a pulse width of 7 ns. The 8 mm-diameter laser beam is focused into the vacuum quartz tube along the axis by a $f = 1200$ mm lens. A Brewster window and a set of five diaphragms with aperture varying between 9 mm and 7 mm diameter have been installed at the entrance and at the exit of the quartz tube to reduce laser stray light. The focal spot size of the laser pulse is approximately 2 mm in diameter. The scattered light is collected through the view port 2 at $z = 50$ cm, in the center of the quartz tube. Reflections from the opposite side of the port at the laser wavelength are significantly reduced by a CuO coating. An $f = 20$ mm, $d = 25$ mm aspheric lens is used to image a 4 mm diameter plasma section into a $910 \mu\text{m}$ optical fiber. The collection volume is, therefore, $\approx 2 \times 2 \times 4 \text{ mm}^3$ and defines the spatial resolution of the measurements. A polarizer is inserted in the collection path to reduce the recorded plasma self-emission. In order to suppress stray light from reflections and Rayleigh scattering, a filter setup based on a volume Bragg grating from OptiGrate, providing a band-width of 0.3 nm with an optical density $\text{OD} = 4$ [31, 32], is used. The light exiting the fiber is collimated using a $d = 50$ mm, $f = 100$ mm aspheric lens. In the present setup, the collimation of the light from the $910 \mu\text{m}$ fiber is not sufficient to reach the specified extinction of OD 4. However, this approach was chosen as a compromise between simple implementation of the optics, optical throughput, and filtering performance. The filtered light is imaged by an $f = 75$ mm spherical lens onto the input slit of a high through-put $f/2$, $f = 200$ mm lens based (Nikon AI 200 mm f2 ED IF) spectrometer, that is equipped with a 2400 l/mm grating. The spectrometer is coupled to a Princeton Instruments PiMax (PM4-1024f-SR-FG-18-P43) gated Intensified Charged Coupled Device (ICCD). The typical gate time is adjusted to 30 ns to record the entire laser pulse and to account for a jitter of ≈ 8 ns in the trigger chain. The system provides a dispersion of $\delta\lambda = 0.024 \text{ nm/px}$. High-resolution measurements with entrance slit width of $200 \mu\text{m}$ yield a spectral resolution of $\Delta\lambda = 0.13 \text{ nm}$. To increase the optical throughput, measurements are typically taken with a $500\text{-}\mu\text{m}$ entrance slit with $\Delta\lambda = 0.4 \text{ nm}$ (flat-top). To achieve an acceptable signal-to-noise ratio (SNR), measurements are averaged over 50 to 200 laser pulses. With the HPS operating

at 0.2 Hz, this results in an effective measurement time of four to 16 min per spatial and temporal point. During the measurement time, the experimental conditions, e.g. the RF power P_{RF} , the argon pressure p , and the DC magnetic field B_0 , exhibit a variation of less than $\pm 2.5\%$. The uncertainty due to the shot-to-shot reproducibility of the experimental parameters during one measurement is well below the statistical uncertainty of the analysis (see section 3.1). Furthermore, the laser intensity is monitored by a fast photo-diode that records a diffuse reflection from one of the mirrors and the obtained TS signal is corrected for potential variations.

3. Experimental results

3.1. TS data analysis procedure

The TS setup described above enables the precise, local measurement of n_e in the HPS, and furthermore provides a measurement of the electron temperature T_e , that was previously inaccessible. Figure 3 illustrates the TS measurement obtained with a spectrometer entrance slit of $500 \mu\text{m}$ and averaged over 100 laser pulses. The data have been acquired at the fifth RF pulse, see figure 2, with $P_{\text{RF}} = 27 \text{ kW}$ (9 kW/antenna), $p = 8 \text{ Pa}$ Argon, $B_0 = 106 \text{ mT}$, and at $t = 350 \mu\text{s}$ after the start of the RF pulse. The data have been corrected for electronic background noise, residual stray light at the laser wavelength, and emission from the plasma. The recorded spectrum has been fitted with a Gaussian distribution function, where the data shown in gray are excluded from the fit. The central region at 532 nm is not taken into account due to remaining laser stray light and distortion effects from the notch filter. The region at 528.7 nm is excluded due to intensity fluctuations of the plasma self emission resulting from the Ar II 4 s - 4p transition. Shown are the best fit as red solid line, as well as the uncertainties from the fit accounting for $1\text{-}\sigma$ in red dashed and dotted lines. In the example shown, the FWHM of 3.47 nm yields an electron temperature of $T_e = 2.0 \text{ eV}$. The scattered intensity was absolutely calibrated using Raman scattering in nitrogen and yields an electron density of $n_e = 2.6 \times 10^{-20} \text{ m}^{-3}$.

The uncertainty of the TS measurement can be estimated as follows. For T_e , the statistical uncertainty from the Gaussian fit ($3\text{-}\sigma$) accounts for typically $\pm 0.1 \text{ eV}$. An uncertainty in the dispersion of 0.002 nm/px causes a systematic error in T_e of 1%, which is negligible in comparison to the statistical uncertainty. For n_e , the statistical uncertainty due to the Gaussian fit is 7%. Additionally, several sources of uncertainty from the absolute calibration have to be taken into account: 1) the reproducibility of the laser energy introduces a statistical uncertainty of 2.5%; 2) the pressure of the N_2 gas used for the calibration was determined with an accuracy of 3%; 3) the theoretical Raman cross sections are known to a precision of 8% [33]; 4) the measured Raman spectrum can be fitted to a precision of 5%; 5) the polarization purity of the laser pulse ($\approx 80\%$) can induce an uncertainty of up to 5% and leads to an underestimation of the measured electron density. Considering all sources

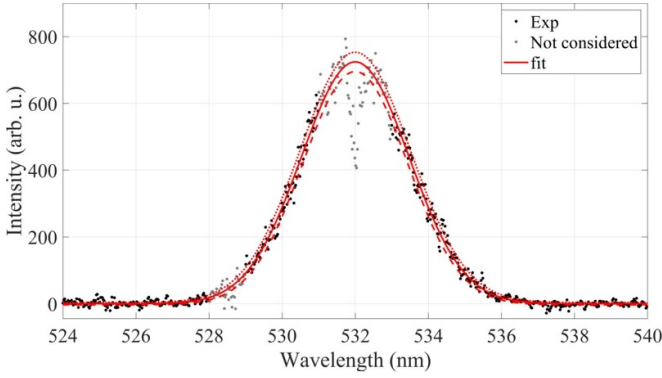


Figure 3. Experimental Thomson scattering (TS) spectrum with Gaussian fit function for $P_{\text{RF}} = 27$ kW, $p = 8$ Pa argon, $B_0 = 106$ mT, $t = 350$ μs yields $n_e = 2.6 \times 10^{-20}$ m^{-3} and $T_e = 2.0$ eV.

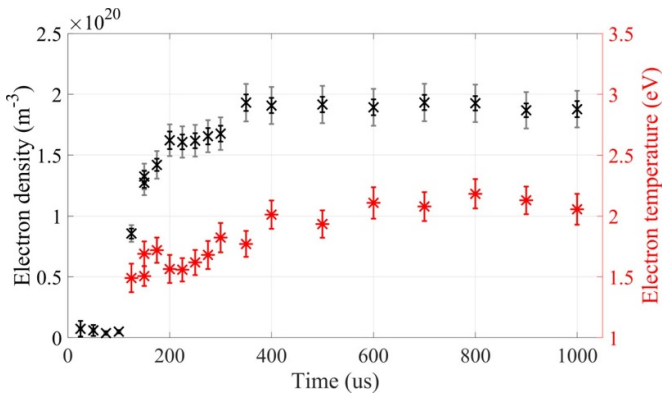


Figure 4. Time evolution of the plasma parameters with $P_{\text{RF}} = 12$ kW, $p = 8$ Pa argon, and $B_0 = 106$ mT. The error bars represent the statistical uncertainties. Additionally, for n_e , a gray error bar shows the systematic uncertainty.

of error to be independent, we can use Gaussian error propagation. Therefore, the statistical uncertainty of n_e accounts for 8.5% while the systematic uncertainty (which is the same for all measurements taken with the same calibration) is -11% and $+10\%$.

3.2. Time evolution of plasma parameters

Figure 4 illustrates the time evolution of the electron density (black symbols) and of the temperature (red symbols) at the center of the HPS for operation parameters $P_{\text{RF}} = 12$ kW (4 kW/antenna), $p = 8$ Pa argon, and $B_0 = 106$ mT. During the first 100 μs after the start of the fifth RF pulse, the electron density is below the sensitivity of the TS diagnostics. Subsequently, n_e increases rapidly to $\approx 1.6 \times 10^{-20}$ m^{-3} at $t = 200$ μs . The peak density of 1.9×10^{-20} m^{-3} is reached at $t = 350$ μs and remains approximately constant until $t = 1000$ μs . The electron temperature ranges between 1.5 eV, at the beginning of the discharge, and increases up to 2.2 eV. At the time of peak density, the electron temperature is typically around 2.0 eV. The minor variation of the plasma parameters after $t = 350$ suggests that a stable plasma condition is

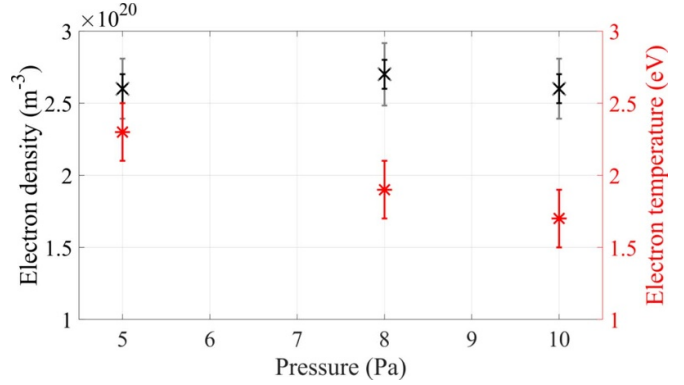


Figure 5. Variation of the plasma parameters with the argon pressure at 27 kW and $B_0 = 106$ mT shows relatively constant density while the electron temperature drops with increasing pressure.

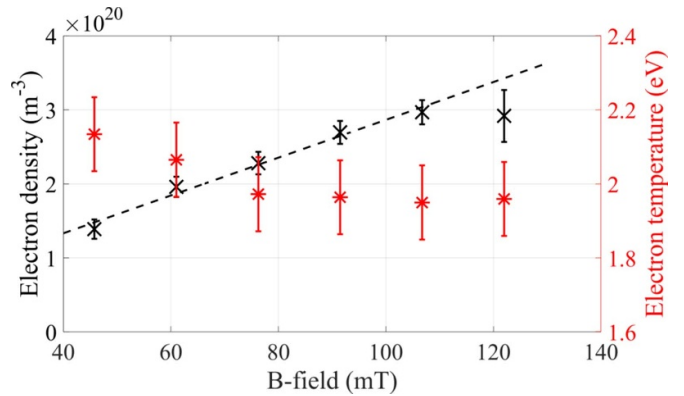


Figure 6. Variation of the plasma parameters with the magnetic field at $P = 27$ kW and $p = 8$ Pa argon, the dashed line shows a linear fit to the density data.

reached and that the plasma can be modeled by a steady-state approximation. Note that the temporal evolution of the plasma parameters changes slightly with the experimental parameters (B -field, power, pressure). In the following, data obtained at the time of peak density, typically between $t = 300$ μs and $t = 350$ μs , are presented.

3.3. Influence of pressure on plasma parameters

The effect of the argon pressure on the plasma parameters in the investigated pressure range is illustrated in figure 5. The presented data indicate a rather small effect of the background gas pressure on the electron density at the center of the plasma column. In contrast, a significant decrease of electron temperature with increasing pressure is observed, which is consistent with the predictions from global 0D models [29, 34] and will be further discussed in section 5.1.

3.4. Influence of magnetic field on plasma parameters

In contrast to pressure, the magnetic field has a large impact on the electron density, as shown in figure 6 for constant power

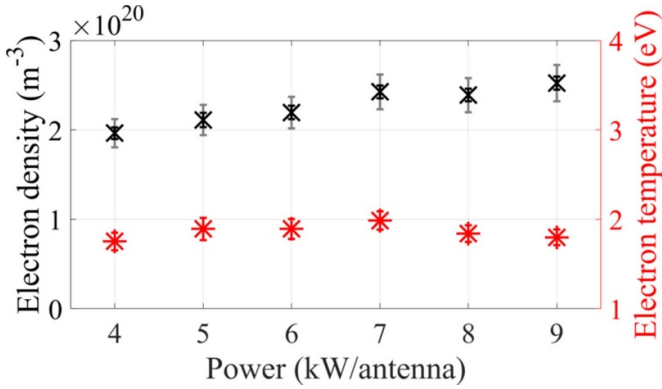


Figure 7. Variation of plasma parameters with the antenna power with $p = 8 \text{ Pa}$, $B_0 = 106 \text{ mT}$. Increasing the discharge power by a factor of 2 increases the electron density by 25%.

and pressure of 27 kW (9 kW/antenna) and 8 Pa, respectively. For B_0 up to $\approx 106 \text{ mT}$, the electron density appears to increase linearly with magnetic field, while at larger field amplitude the density saturates. This correlation was also observed previously [28] and attributed to the classical dispersion relation of helicon waves [35],

$$\omega = \frac{kk_{\parallel} B_0}{q \mu_0 n_e}, \quad (1)$$

where ω is the wave's angular frequency, k and k_{\parallel} are the norms of the total and the parallel (to the DC magnetic field) wave vectors, respectively, q is the electron charge, and μ_0 the vacuum permeability. For a wave excitation at constant frequency $f = \omega/2\pi$ at 13.56 MHz, the electron density is proportional to the magnetic field, given that the wave configuration, kk_{\parallel} , is constant. This relation holds as long as the helicon wave frequency is larger than the lower hybrid frequency $\omega > \omega_{\text{LH}} \approx \sqrt{\omega_{ce}\omega_{ci}}$, where ω_{ce} and ω_{ci} are the electron and ion cyclotron frequencies, respectively. For a driving frequency of 13.56 MHz, ω_{LH} is reached at a magnetic field as high as 132 mT, which could, therefore, explain the flattening of the density curve at large B -fields. However, applying the helicon approximation to the present experiment is clearly an oversimplification of the system (perfectly conducting boundary, homogeneous electron density, no collisions). Moreover, previous results showed that in case of a weakly bounded helicon plasma, the axial wavelength is not constant but adjusts smoothly to the applied B -field and density [36]. In this case, the geometric configuration of the experiment is clearly not imposing the wave vector geometry ($kk_{\parallel} = \text{const}$) of the helicon wave.

3.5. Influence of RF power on plasma parameters

The variation of the plasma parameters with the power delivered to each antenna is illustrated in figure 7. The power was varied from 4 kW/antenna to 9 kW/antenna and the matching network of the three antennas was optimized individually for each power. Note that the data presented in

figures 7 and 6 were obtained several months apart from each other. Consequently, additional changes in the HPS setup had a discernible impact on the absolute electron density. Nonetheless, the trends depicted remain valid. Figure 7 shows that the electron temperature is rather constant over the probed power range, while the electron density increases slightly. In particular, a doubling of the RF power results in an increase of the electron density of 25% from $2 \times 10^{-20} \text{ m}^{-3}$ to $2.5 \times 10^{-20} \text{ m}^{-3}$. The rather moderate increase of density at this high power level might be related to the phenomenon of neutral depletion [37], which may affect the plasma density at ionization degrees as low as 1%. Further investigation of the transport of ions and neutrals, for example by LIF [24], is highly desired to understand the impact of these phenomena on the HPS. Additional effects potentially related to a flattening of the electron density will be discussed in section 5.3.

4. Modelling

To interpret our experimental results and to comprehend the effect of the main physical processes on the establishment of the steady-state plasma parameters, we developed a 1D power and PPM. The model allows us to assess the general trends observed in the experiment and whether the measured plasma parameters are consistent with the collisional power deposition of the helicon wave. We first calculate the propagation of the helicon wave and the power density deposited into the plasma using a predefined plasma profile as an input to the simulation. The power density profile is integrated over the azimuthal and radial coordinates and used as input for the 1D (z -direction) PPM. We use the fluid equations to balance this source of energy and of charged particles with the losses at the plasma boundary. The power and particle balance equations are solved numerically to find the axial distributions of n_e and T_e in the established steady state. The electron density profile retrieved from the simulation results is used as new input for the wave propagation calculation. We find that the model converges after only a few (3–4) iterations. While the non-homogeneous features of the simulated electron density slightly increase after several iterations, we show here only the first iteration, as the increased computation time does not justify the gain in precision, especially taking into account the limited experimental data. In section 4.1, we first outline the calculation of the helicon wave propagation and of its power deposition. This is followed by the description of the PPM in section 4.2.

4.1. Modeling the propagation of the helicon wave

In order to simulate the propagation of the helicon wave in plasma and deduce its power density, we solve Maxwell's equations with a time harmonic ansatz $\vec{X}(\vec{r}, t) = \vec{X}(\vec{r})e^{-i\omega t}$ and describe the plasma medium by a complex conductivity tensor.

Using the time harmonic ansatz, Maxwell's equations can be combined to yield the wave equation

$$\vec{\nabla} \times \vec{\nabla} \times \vec{E} = \mu_0 \omega^2 \epsilon \vec{E}, \quad (2)$$

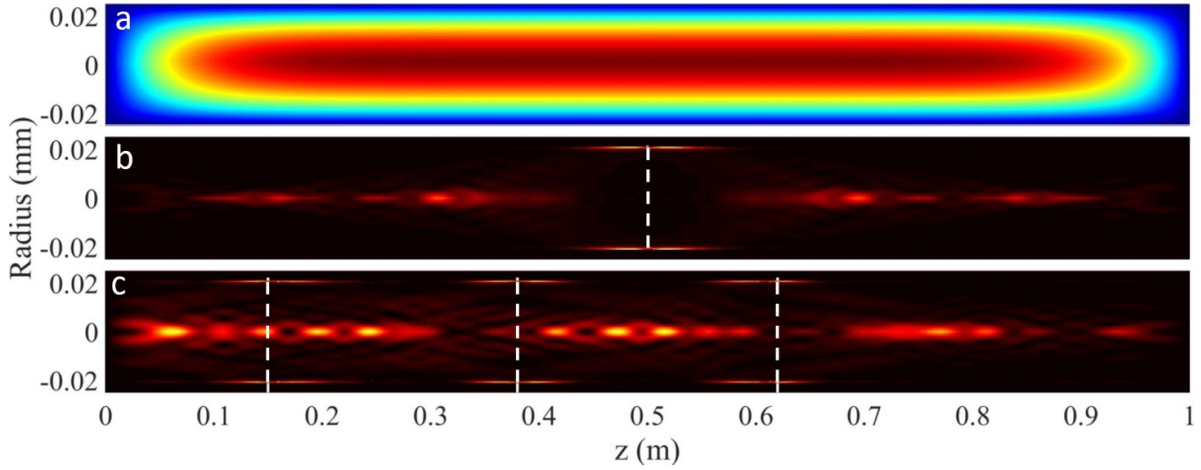


Figure 8. 2D power deposition maps (a) electron density profile used for power deposition calculation, (b) power deposition for 1 ring antenna at $z = 0.5$ m, (c) power deposition for 3 antennas as in the present HPS setup.

where ϵ is the complex dielectric tensor describing the response of the plasma. A constitutive relation for the plasma medium (Ohm's law) can be found from the first moment of Boltzmann's equation (momentum conservation) for the electron fluid:

$$m_e \partial_t \vec{u} + q \vec{E} + q \vec{u} \times \vec{B}_0 + \nu_{en} m_e \vec{u} = 0, \quad (3)$$

where \vec{u} represents the mean fluid velocity, m_e the electron mass, \vec{E} the oscillating electric field, \vec{B}_0 the background magnetic field aligned to the z -direction, and ν_{en} the effective electron-neutral collision frequency. Equation (3) represents a classical, collisional model that is equivalent to the concept of Ohmic heating. Defining the current density as $\vec{j} = -qn_e \vec{u}$ and using the time harmonic ansatz, we can re-write equation (3) as

$$\vec{E} = \frac{1}{\epsilon_0 \omega_{pe}} \left[\hat{\omega} \vec{j} + \omega_{ce} \vec{j} \times \vec{e}_z \right], \quad (4)$$

where we introduce the plasma angular frequency of electrons $\omega_{pe} = \sqrt{q^2 n_e / \epsilon_0 m_e}$, the electron cyclotron frequency $\omega_{ce} = q B_0 / m_e$, and the complex frequency $\hat{\omega} = \nu_{en} - i\omega$. Note, that we did not use the approximations common in helicon physics to derive equation (4). In particular, we did not assume a constant electron density, perfectly conducting boundaries, or negligible collisionality. Accordingly, we can estimate the power deposition into the plasma due to the collisions.

Equation (4) is equivalent to Ohm's law $\vec{j} = \sigma \vec{E}$ with the complex conductivity tensor

$$\sigma = \frac{\epsilon_0 \omega_{pe}^2}{\hat{\omega}^2 + \omega_{ce}^2} \begin{pmatrix} \hat{\omega} & -\omega_{ce} & 0 \\ \omega_{ce} & \hat{\omega} & 0 \\ 0 & 0 & (\hat{\omega}^2 + \omega_{ce}^2) / \hat{\omega} \end{pmatrix}, \quad (5)$$

which yields the complex dielectric tensor

$$\epsilon = \epsilon_0 \left[1 + \frac{\sigma}{-i\omega \epsilon_0} \right]. \quad (6)$$

Inserting equation (5) into equation (2), the wave equation is solved numerically. Therefore, the detailed HPS geometry was modeled in COMSOL [38] electromagnetic module and an initial electron density, shown in figure 8 a, was defined. For our convenience, we impose a radial electron density profile throughout this paper that follows the power law

$$n_e(r) = n_0 \left(1 - \frac{r^n}{R_p^n} \right), \quad (7)$$

where R_p is the radius of the plasma boundary and n_0 the electron density on-axis. This electron density profile can easily be integrated radially and allows to establish a simple expression for the following 1D PPM. In the present work, we set $n = 2$ to achieve a parabolic density profile. In axial direction, the initial electron density distribution is defined as flat, $n_0(z) = \text{const}$, and to fall off parabolically at the boundary.

The principal output of the wave calculation further used for the PPM is the deposited power mapping, generally expressed as:

$$Q_{\text{wave}}(r, z) = \frac{1}{2} \left[\vec{j}^* \cdot \vec{E} + \vec{j} \cdot \vec{E}^* \right]. \quad (8)$$

It was found in 3D calculations, performed with a ring antenna configuration, that the resulting wave presents a very clear $m = 0$ feature with azimuthal invariance. We, therefore, switch to a 2D calculation that provides a higher precision, as it allows for a denser mesh than in the 3D simulation. The results of this 2D simulated power deposition are shown in figure 8. Figure 8(a) illustrates the initial electron density map with a peak value $n_0 = 2.6 \times 10^{-20} \text{ m}^{-3}$ at a background gas pressure of 8 Pa. In figure 8(b) we show the resulting 2D power deposition for a single antenna. The power transfer efficiency to the plasma, accounting for the resistance of the antenna, was considered and found to be $\geq 80\%$. The power deposition profile is axially symmetric around the antenna position, as expected for an $m = 0$ ring antenna, and exhibits an axial wavelength of ≈ 5 cm. The radial profile changes drastically

with the distance from the antenna. At the antenna position, the main power is deposited close to the plasma edge by modes that are characterized by short radial (and axial) wavelengths, as well as strong radial damping. These modes can be identified as belonging to the Trivelpiece-Gould (TG) family [39]. Further away from the antenna, the power deposition peaks on-axis, due to dominant helicon H-modes that are characterized by a radial wavelength comparable to the radius of the vacuum tube.

In figure 8(c) we extend the calculation to the actual geometry of the HPS with three antennas. The interaction of the antennas with each other manifests itself in the development of distinct interference patterns. At the antenna positions, increased power deposition at the outer plasma boundary is observed, as expected from the 1-antenna calculation. Additionally, the waves propagating from the neighboring antennas lead to some power deposition also on-axis at the antenna positions. Asymmetries in the axial directions are caused by the lack of symmetry in the boundary conditions of the present setup of the HPS.

4.2. Power-and-particle balance

After we have calculated the power deposited by the helicon wave, we can use a PPM to evaluate the resulting electron density n_e and temperature T_e . We use here Q_{wave} as a source for the electron fluid temperature, and, as a consequence, for ionization. This source of particles and power is balanced by the losses of the charged particles and their associated energy at the plasma boundary. We, therefore, need to evaluate the particle's energy and flux (perpendicular to the boundary) at the boundary. In axial direction, we use the model of ambipolar diffusion, where the particle flux results from the fluid equations. In radial direction, we employ a floating sheath model that defines the particle density and velocity at the sheath entrance. We can then solve the particle and the power balance equations to find the 1D steady-state axial profiles of n_e and T_e .

We consider the particle flux $\vec{\Gamma} = n\vec{u}$

$$\vec{\nabla} \cdot \vec{\Gamma} = k_i(T_e)n_g n_e, \quad (9)$$

where the source term is due to electron impact ionization with k_i the (strongly dependent on electron temperature) rate coefficient for ionization and n_g the neutral gas density.

In axial direction, we consider a particle flux Γ_z due to ambipolar diffusion, so that $\Gamma_z = -\mu_i \partial_z p_e$, where we assume that the ion temperature T_i and the ion mobility μ_i are much smaller than their electronic counterparts T_e and μ_e : $T_i \ll T_e$ and $\mu_i = q/m_i \nu_{in} \ll \mu_e = q/m_e \nu_{en}$ [34]. Both, ions and electrons, are, therefore, moving at the same velocity and $\vec{\Gamma}_i = \vec{\Gamma}_e = \vec{\Gamma}$. Here, $m_{i,e}$ is the mass of electrons and ions and $\nu_{in,en}$ is their effective collision frequency with neutrals. At the boundary ($z=0$ and $z=1$ m) of the simulation domain, the losses are defined by the particle flux at the sheath entrance $\Gamma_z(0) = \Gamma_z(1) = n_{\text{sh}} u_{\text{Bohm}}$ [40], given by the particle density

at the sheath entrance $n_{\text{sh}} = n_0 e^{-1/2}$ and the Bohm velocity $u_{\text{Bohm}} = \sqrt{qT_e/m_i}$, where T_e is given in Volt.

In order to describe the losses in radial direction, the sheath model has to be modified due to the presence of the magnetic field that confines the particles to some degree. Therefore, we introduce the *screening factor*, $f_\xi < 1$, to account for the reduction of the radial transport and of particle losses [40]

$$\begin{aligned} \Gamma_r(R_p) &= n_{\text{sh}}^B u_{\text{sh}}^B = f_\xi n_{\text{sh}} u_{\text{Bohm}} \\ &= f_\xi n_0 e^{-1/2} \sqrt{\frac{qT_e}{m_i}}. \end{aligned} \quad (10)$$

We can now integrate over the particle flux using Gauss' divergence theorem

$$\int_{\Delta S} \vec{\Gamma} d\vec{S} = \int_{\Delta V} \vec{\nabla} \cdot \vec{\Gamma} dV = \int_{\Delta V} k_i n_g n_e dV. \quad (11)$$

The integration volume is the cylindrical elementary volume $\Delta V = \int_0^{2\pi} \int_0^{R_p} \int_z^{z+\Delta z} r dr dz = \pi R_p^2 \Delta z$ at location z . When integrating over the bases of the elementary volume, we use the electron density profile from equation (7) that we can integrate easily as $\int_0^{R_p} 2\pi r (1 - r^n/R_p^n) dr = 2\pi f_n R_p^2$ with $f_n = n/(2n+4)$. Thus, we find

$$\mu_i \partial_z^2 p_0 = n_0(z) \left(\frac{\xi u_{\text{Bohm}}}{f_n R_p} - k_i n_g \right), \quad (12)$$

where we defined $\xi = f_\xi e^{-1/2}$. The left hand side of equation (12) results from the surface integral over the two bases of the cylindrical volume element at z and $z + \Delta z$, where $p_0 = k_B n_0 T_e$ is the thermal pressure on axis. The first term on the right hand side (RHS) of equation (12) represents the surface integral over the lateral surface of the elementary volume element. The volume integral of equation (11) corresponds to the second term on the RHS of equation (12). Equation (12) illustrates that the axial particle flux, which is determined by the ion mobility and the pressure gradient along the axis, is driven by ionization and losses on the lateral cylinder surface.

Similarly, we consider the energy flux conservation

$$\begin{aligned} \vec{\nabla} \cdot \vec{\Gamma}_W &= Q_{\text{wave}} - n_e n_g (k_i(T_e) \epsilon_i + k_e(T_e) \epsilon_e \\ &\quad + k_m(T_e) \epsilon_m). \end{aligned} \quad (13)$$

The energy flux is closely related to the particle flux through the energy associated to the fluid: $\vec{\Gamma}_W = \alpha T_e \vec{\Gamma}$, where $\alpha = 5/2$. The energy flux is driven by the source of the energy deposition by the helicon wave Q_{wave} and the energy loss terms due to ionization (i), excitation (e), and elastic collisions (m), where $k_{i,e,m}$ and $\epsilon_{i,e,m}$ denote the rate coefficient and the energy for those processes, respectively. Note, that k_m is related to the collision frequency by $\nu_{en} = k_m n_g$.

We use here Q_{wave} from section 4.1 and define the integral of the deposited power over the radial coordinate

$$\tilde{Q}_{\text{wave}}(z) = \int_0^{R_p} r' Q_{\text{wave}}(r', z) dr'. \quad (14)$$

By using Q_{wave} from the calculation of the wave propagation, we assume that the helicon plasma is fully sustained by collisional dissipation. Note that in the helicon physics community, other dissipation mechanisms, such as Landau damping [41–43], for which no analytic expressions exist, have been suggested. These could be accounted for, in principle, in the present model by using an effective collision frequency ν_{en}^{eff} .

We can now formulate

$$\begin{aligned} \alpha \int_{\Delta S} T_e \vec{\Gamma} \, d\vec{S} &= \int_{\Delta V} \vec{\nabla} \cdot \vec{\Gamma}_W \, dV \\ &= \int_{\Delta V} \left[Q_{\text{wave}} - n_e n_g \sum_p k_p \epsilon_p \right] dV, \end{aligned} \quad (15)$$

with $p = i, e, m$, and integrate over the elementary volume in the same way as in equation (12)

$$\begin{aligned} \alpha \mu_i \partial_z (T_e \partial_z p_0) &= -\frac{\tilde{Q}_{\text{wave}}}{f_n R_p^2} + n_0(z) \frac{\alpha \xi u_{\text{Bohm}} T_e}{f_n R_p} \\ &\quad + n_0(z) n_g (k_i \epsilon_i + k_e \epsilon_e + k_m \epsilon_m), \end{aligned} \quad (16)$$

with \tilde{Q}_{wave} given by equation (14). The source term of electrons in the particle balance is associated with a loss term in the energy balance, as the system depletes energy in order to provide the binding energy the electron needs to overcome. Additionally, the energy balance contains the source of energy of the deposited power and loss terms originating from excitation (the power is then radiated) and elastic collisions (energy transfer to neutrals). The elastic collision energy is given by $\epsilon_m = 3qT_e m_e / m_i$.

The two coupled equations (12) and (16) are solved jointly in COMSOL with a finite elements method to retrieve the on-axis electron density $n_0(z)$ and temperature $T_e(z)$.

Figure 9 shows the simulation results for $p = 8$ Pa, $P = 27$ kW (9 kW/antenna), $B_0 = 106$ mT, and an initial electron density of $2.6 \times 10^{20} \text{ m}^{-3}$, in comparison with the experimental results. Figure 9(a) summarizes the setup with the positions of the antennas (orange), the optical ports (blue), and the magnetic field coils (green). In black, the axial distribution of the DC magnetic field is shown. To label the cases with different magnetic fields, we use the peak value at $z = 40$ cm.

Figure 9(b) provides the collisionally deposited power from integration of figure 8(c) over the radius r and represents the term \tilde{Q}_{wave} in equation (16). Due to the integral in equation (16), the model does not resolve the radial distribution of the power deposition given in figure 8. Towards the plasma edges, the power deposition falls off rapidly due to the decreasing B -field. The asymmetry between the left and right edges of the system is caused by the asymmetric B -field distribution, as well as the different distances to the boundary of the simulation domain (equivalent to the glass tube in the experiment), with respect to the central antenna (antenna no 2 at $z = 37$ cm). The double peak at antenna 2 is caused by interference effects between the three waves. It is evident that the present HPS setup with three antennas and a rather inhomogeneous B -field leads to a highly inhomogeneous and asymmetric power deposition. The effect of an improved symmetry

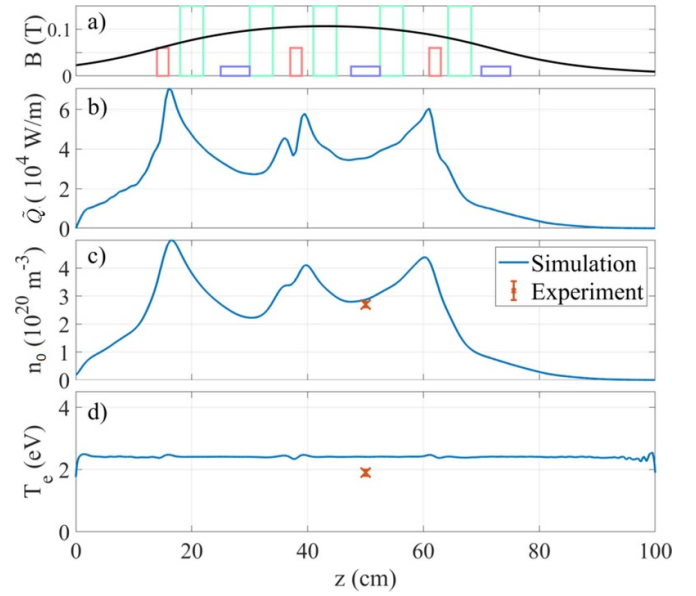


Figure 9. Simulation results for $p = 8$ Pa, $P = 27$ kW, $B_0 = 106$ mT, showing the initial configuration, the deposited power integrated over r and θ , the on-axis electron density n_0 , and the on-axis electron temperature T_e .

of the setup on the deposited power and electron density will be assessed in section 5.4.

The on-axis electron density n_0 , calculated with the 1D PPM, is shown in figure 9(c). The axial distribution of n_0 closely resembles the power deposition of figure 9(b). Fine details of the power distribution, for instance at $z \approx 40$ cm, are smoothed out by transport processes. As expected, the amplitude of the simulated electron density profile is very sensitive to the particle loss rate at the cylinder surface. We here use the screening factor f_ξ as a tuning parameter to reproduce the measured electron density. For the magnetic field of $B_0 = 106$ mT, a value of $f_\xi = 0.4$ could well reproduce the experimental electron density at $z = 50$ cm. Note that the screening coefficient f_ξ also has a small effect on the simulated temperature.

The 1D simulation suggests that the axial profile of the electron density is not homogeneous but rather peaked at the antenna positions with a variation of a factor of more than two along the axis. However, comparison of $\tilde{Q}_{\text{wave}}(z)$ (figure 9(b)) with $Q_{\text{wave}}(r, z)$ (figure 8) shows that at the antenna position, a large fraction of the power is deposited at the plasma boundary by TG dominated modes. Due to the large radius, this contribution dominates the integrated power shown in figure 9(b), although the power actually deposited on axis is rather small. Therefore, the simulated 1D electron density at the antenna positions is probably an overestimation. Radially resolved simulations, as well as additional measurements closer to the antenna positions, are planned to address this issue.

In figure 9(d) we show the simulated electron temperature T_e . The temperature of the system adjusts to provide a high enough ionization rate to balance the losses. Therefore, the simulated temperature is highly sensitive to the value of the

ionization rate k_i . Here, we use the rates given by Lieberman [34] which reproduce the experimental value of T_e within 25%. When using the ionization rate coefficients provided by Bolsig+ [44], for instance, the temperature was simulated to be ≈ 4 eV instead of the measured ≈ 2 eV. The electron density, on the other hand, is only effected slightly by the choice of k_i in the PPM.

In contrast to the electron density, the electron temperature is rather constant along the axis. Thermal diffusion, representing an energy transport process, is related to the electron mobility and thermal velocity. In contrast, particle diffusion, which requires mass transport, is limited by the ion mobility in the model of ambipolar diffusion. We can estimate the time scale of thermal diffusion τ_{th} as follows:

$$\tau_{\text{th}} = \frac{L^2}{\chi} = \frac{C_e n_0}{\kappa} L^2 = \frac{3/2 k_B n_0}{\kappa} L^2 \quad (17)$$

with L the typical length scale of diffusion, χ the electron thermal diffusivity, C_e the specific heat capacity of electrons, and κ their thermal conductivity given as [45]

$$\kappa [\text{erg s}^{-1} \text{cm}^{-1} \text{K}^{-1}] = \frac{1.93 \times 10^{-5} \zeta(Z) T_e [\text{K}]^{5/2}}{Z \ln \Lambda}. \quad (18)$$

Here, $\ln \Lambda \approx 5$ is the Coulomb logarithm and $\zeta(1) = 0.95$ is a numerical factor depending on the average charge Z . Assuming a diffusion length of 10 cm, an electron temperature of 2 eV, and an electron density of $2 \times 10^{-20} \text{ m}^{-3}$, the typical thermal diffusion time is $\tau_{\text{th}} \approx 20 \mu\text{s}$. This estimate demonstrates that we expect a fast equilibration of the electron temperature over the entire simulation domain and a flat temperature profile in steady state, therefore. The time scale of particle diffusion is given as $\tau_{\text{part}} = L^2/D_A$ with

$$D_A = D_i \left(1 + \frac{T_e}{T_i} \right) = \frac{k_B T_i [\text{K}]}{m_i \nu_{in}} \left(1 + \frac{T_e}{T_i} \right), \quad (19)$$

where D_i and D_A are the diffusion coefficients for ions and for ambipolar diffusion, respectively. Utilizing $T_i = 0.1$ eV, $T_e = 2$ eV, and $\nu_{in} \approx 1$ MHz, resulting from an ion-neutral collision cross section of 10^{-18} m^2 at $p = 8$ Pa, the particle diffusion time over a distance of 10 cm yields $\tau_{\text{part}} \approx 2$ ms. In the present regime, particle diffusion is two orders of magnitude slower than thermal diffusion, which explains the significant difference in the electron density and temperature profiles.

5. Simulation results for parameter scans

In section 4 we used the measured n_e and T_e for the experimental case of $p = 8$ Pa, $P = 27$ kW, and $B_0 = 106$ mT to adjust the variable parameters of the model (ionization rate coefficient k_i and screening coefficient f_ξ). In the following we will use these determined *model* parameters and vary the *experimental* parameters (p , P , and B_0). The *plasma* parameters, n_e and T_e , predicted by the model, can then be directly compared to the measurements presented in section 3.

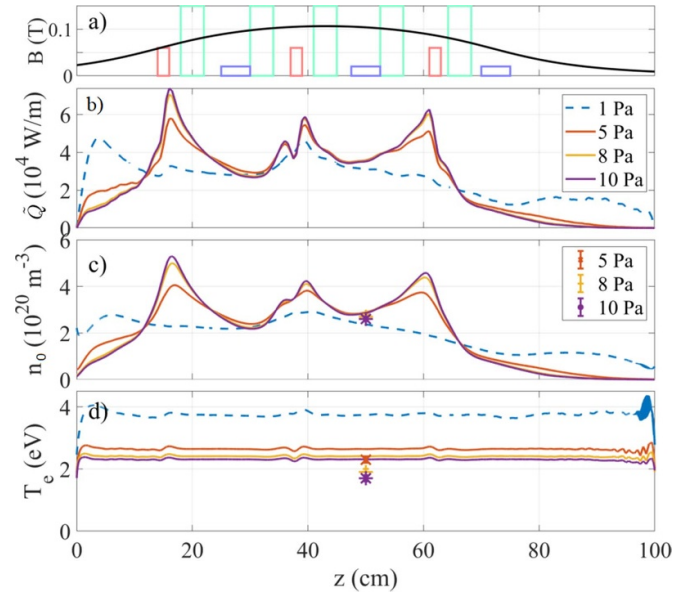


Figure 10. Simulation results for $p = 1$ Pa to 12 Pa, $P = 27$ kW, $B_0 = 106$ mT. The simulation reproduces the seemingly constant n_e at the measurement position, as well as the trend of the temperature measurement.

5.1. Pressure variation

Figure 10 shows the results of the simulation for different initial gas pressures. It is evident that the simulation reproduces the trend of the experimental values of n_e and T_e very well. The change in the collisionality of the plasma with the varying background gas pressure has several effects: i) The increased collisionality at higher pressure leads to a larger damping of the wave so that more power is deposited in the antenna region, as seen in figure 10(b). ii) At lower pressure, the increased mobility of the particles leads to a smoothing of the electron density profile (see figure 10(c), $p = 5$ Pa, $z \approx 40$ cm). Surprisingly, at $z = 50$ cm, where the measurements were performed on optical port 2, the simulated electron density is indeed independent of the pressure, as observed in the experiment. iii) The ionization rate increases linearly with gas pressure, while k_i , in the present parameter range, increases faster than linearly with T_e . An increase of the background pressure, therefore, leads to a decrease in T_e , as also shown in [34, 37].

Due to the homogeneous electron temperature, the 2D PPM exhibits many similarities to global 0D models [34]. In those models, for weakly ionized plasmas, the power balance and the particle balance can be decoupled. The electron temperature then solely depends on the neutrals density and a form factor that relates the surface of the vacuum vessel (boundary losses) to its volume (ionization volume). However, it is independent of electron density. The electron density, on the other hand, is proportional to the deposited power. The increase of the electron temperature with a decreasing background pressure predicted by the simple 0D model in the present parameter range close to the ionization threshold is well reproduced by the 1D model and verified by the experimental measurements.

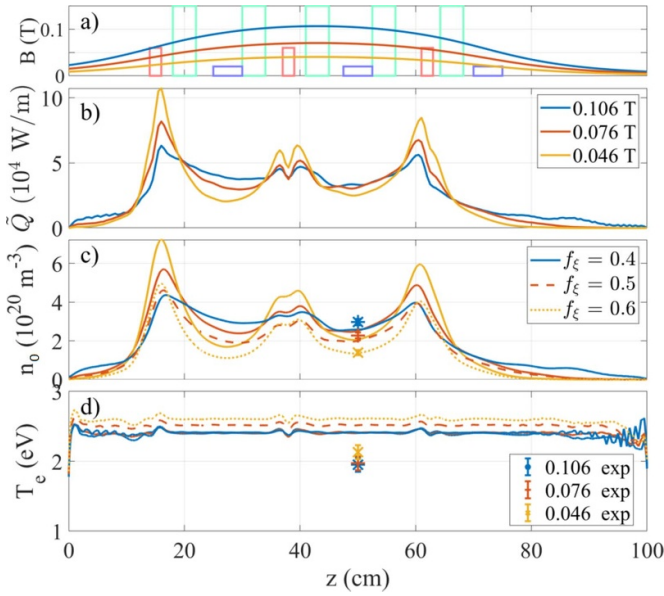


Figure 11. Simulation results for $p = 8$ Pa, $P = 27$ kW, $B_0 = 46$ mT to 106 mT. The simulations demonstrate the large impact of the B -field on the axial profile of the electron density due to the changing propagation of the helicon waves.

To test the effect of a strongly decreased collisionality, another simulation was performed for a gas pressure of 1 Pa. This resulted in a significantly more uniform density profile, mainly caused by a drastic change in the power deposition due to reduced damping. However, at such low pressure, the electron temperature is strongly elevated and the resulting electron density exceeds the gas density. In order to correctly account for this scenario, cross sections for ionization of Ar II (singly ionized argon) to Ar III (two times ionized argon) would need to be considered. Note also that additional effects, like increased energy and particle transport across the B -field at higher pressure and effects of the radial profile on the power deposition, are not taken into account in the present simulation.

The measurements presented with different neutral pressures illustrate the importance of the collision frequency and transport effects on the development of the equilibrium n_e and T_e profiles. This highlights the importance of a combined density and temperature diagnostics to understand the basic physical phenomena that govern the establishment of the electron density in the HPS. In the future, we are planning to investigate a larger pressure range and to obtain detailed radial and axial plasma parameter profiles.

5.2. B -field variation

Figure 11 illustrates the effect of varying the DC magnetic field from $B_0 = 46$ mT to $B_0 = 106$ mT on the simulation results. The initial electron density was set to $2.3 \times 10^{20} \text{ m}^{-3}$ to represent the range of measurement results with different magnetic field. At lower B -field strengths, the primary area of power deposition is near the antennas. Conversely, a higher

B -field facilitates wave propagation into the gap between the antennas, and power deposition in this region, consequently (figure 11(b)). The variation of the B -field strongly impacts the electron density at the inter-antenna area ($z \approx 25$ cm and $z \approx 50$ cm), in particular, at the optical view-port. Here, an increased B -field generally correlates with higher electron densities, as indicated by the solid lines in figure 11(c), where we assumed a fixed screening coefficient, $f_\xi = 0.4$. Consistently, the line-integrated electron density $N_0 = \int n_0(z) dz$, remains practically unchanged across the different B -field values when f_ξ is held constant. Similarly, the simulated electron temperature T_e (figure 11(d)) shows no significant variation with magnetic field strength, assuming a constant f_ξ .

Additionally, we show the effect of an increasing screening coefficient to account for increased losses at the plasma boundary for lower magnetic fields, namely using $f_\xi = 0.5$ for $B_0 = 76$ mT (dashed lines) and $f_\xi = 0.6$ for $B_0 = 46$ mT (dotted lines) in figures 11(c) and d. With these adjustments, a reduced magnetic field results in a notable decrease in the overall electron density, accompanied by a slight increase in temperature. The latter can be understood from the analogy with the 0D model, where the reduced confinement acts like an increased surface of the vacuum vessel, which leads to a reduction of the electron temperature. The adjustment of the screening coefficient for varying magnetic field strengths allows for a precise reproduction of experimental density values at the central view port (markers in figure 11(c)), as well as the observed trend of variation in temperature (markers in figure 11(d)).

The observed linearity between n_e and B_0 at the view port was in principle reproduced in the simulations by variation of the screening coefficient to increase the losses at lower magnetic field. However, figure 11 demonstrates that the relation $n_e \propto B_0$ inferred from the helicon dispersion relation, equation (1), does not hold in general, as seen at the antenna positions, for instance. Nonetheless, a correlation of the screening coefficient f_ξ with B_0 is of course expected. Considering the particle velocity at the sheath entrance, we can formulate an effective electron mass $m_e^{\text{eff}} = (1 + \omega_{ce}^2/\nu_{en}^2) m_e$ due to the magnetic field. The effective Bohm velocity then becomes [40, 46]

$$u_{\text{sh}}^{B_0} = u_{\text{Bohm}}^{\text{eff}}(B_0) = \sqrt{\frac{q(T_i + T_e)}{m_i^{\text{eff}} + m_e^{\text{eff}}}} \approx \sqrt{\frac{m_i}{m_i + \frac{q^2 B_0^2}{m_e \nu_{en}^2}}} u_{\text{Bohm}}. \quad (20)$$

We could associate f_ξ directly with the effective Bohm velocity $f_\xi = \Gamma_r(B_0)/\Gamma_r(B_0 = 0) = u_{\text{Bohm}}^{\text{eff}}(B_0)/u_{\text{Bohm}}$, which would yield an approximately inverse proportionality of f_ξ with B_0 , as roughly suggested by the simulations. However, we assume here that the magnetic field has no effect on the electron density at the sheath entrance, i.e. $n_{\text{sh}}^{B_0} = n_{\text{sh}}$. Moreover, the effective Bohm velocity also strongly depends on the collision frequency in the plasma, which is not well known. Therefore, additional investigations are required to correctly

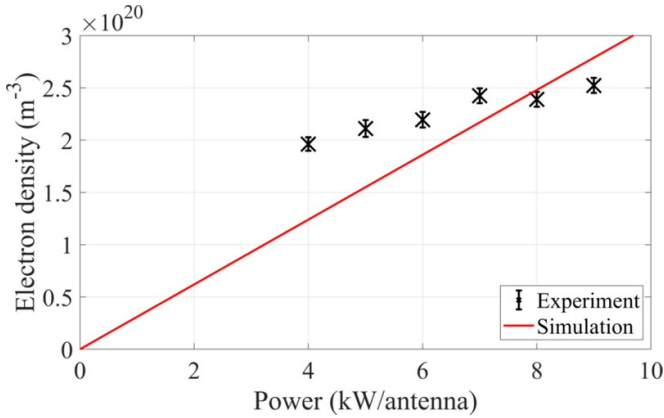


Figure 12. Simulated electron density results for $p = 8$ Pa, $B_0 = 106$ mT and $P_{\text{RF}} = 0$ kW to 27 kW at view port 2 position. The simulation results in a linear relation between input power and electron density while the simulated temperature is constant. In order to describe the saturating behavior of the measured electron density, the model has to be further refined.

account for the effect of the magnetic field in the simulations. Additional measurements at different magnetic fields, and, in particular, for zero magnetic field, that can access the plasma at the antenna positions are planned to further investigate the dependencies of the plasma parameter distributions on the B -field and to benchmark the 1D simulations.

5.3. Power variation

The variation of input power was assessed in the simulation and resulted in a linear relation between power and electron density, as shown in figure 12 (red line). When assuming the same initial electron density profile, the power provided to the antennas occurs in the wave propagation simulation merely as a constant factor for the dissipated power. Similarly, with the present assumptions, the PPM results in a linear relation between dissipated power and electron density, as in the 0D global models [34]. However, several physical phenomena that can lead to a saturation of the achieved electron density when power is increased, as illustrated by the experimental data in figure 12 (black symbols), have been neglected in the present, simple, model. (i) The variation of the initial electron density level will slightly change the power deposition profile. However, the effect is rather small and was not taken into account here, therefore. (ii) The power deposition profile also strongly depends on the radial electron density profile, particularly the density gradient at the boundary. Steeper gradients, associated with higher densities, can result in significant edge power deposition and, therefore, reduce the on-axis density. This scenario was tested by increasing the gradient in the initial radial electron density profile, i.e. setting $n = 8$ in equation (7), and resulted in a lower \bar{Q}_{wave} in the inter-antenna region. (iii) In the present model, a constant neutral density was assumed. Effects of depletion of neutrals due to ionization (here $\approx 10\%$) and the neutrals pressure balance are not taken into account. According to Fruchtmann *et al* [37], an

ionization degree as low as 1% can have a significant effect on the axial electron and neutral density profiles. The sink of neutrals establishing in the plasma center due to the pressure balance reduces the drag on the ions that are no longer confined axially. Therefore, an increase in power can in principle lead to a decrease in electron density. (iv) All loss mechanisms considered in the present model are linear in electron density. At increasing density, however, also three-body-recombination ($\propto n_e^2$) should be taken into account.

Note that the good agreement between measurement and simulation at high power was achieved by adapting the variable model parameters (in particular f_ξ) to the high-power operation. Fixing these parameters while neglecting the aforementioned processes leads to an underestimation of the achievable density at the lower-power operation, as seen in figure 12. In order to further investigate the exact impact of these processes on the plasma, they will be included in a future version of the PPM. Furthermore, extending the measurements to the low-power regime and obtaining radial, as well as axial, density profiles is desirable.

5.4. Study of density uniformity

The most stringent requirement for the AWAKE *accelerator* plasma source is the homogeneity of the axial density profile of 0.25%. We here explore the achievable density homogeneity within the limits of the 1D simulation with an optimized HPS setup. We choose a target density of $2.3 \times 10^{-20} \text{ m}^{-3}$ in order to be close to the experimental conditions that have been used to establish the simulation. A B -field of 0.1 T, constant along the entire simulation domain, is assumed. For these conditions, a single ring antenna excites a dominant mode with axial wavelength of 5 cm. Therefore, an antenna was placed every 5 cm along the ideal quartz tube. The overall 12 antennas are powered with 25 kW in total (2.1 kW/antenna) and the argon pressure is set to 8 Pa. Figure 13(a) shows the 2D deposited power map. An axial line-out at the center (figure 13(b)) illustrates a flat power deposition region in the central 0.5 m with an oscillation of 25 mm period and 10% amplitude in comparison to the average value. Integration over the radial variable (figure 13(c)) reduces the amplitude of the oscillations but introduces an over-all gradient resulting in a slightly lower power deposition in the center of the system. Figure 13(d) shows the resulting electron density from the PPM (black line), compared to the original density profile utilized to calculate the power deposition (red line). The mobility of the particles smooths out the oscillations but the density gradient seen in figure 13(c) is still present. We achieve here an axial variation of the electron density of $\pm 10\%$ over the central 0.5 m of the HPS. This is a significant improvement over the $\pm 50\%$ density variation predicted for the present experiment (3 antennas, strongly varying axial B -field), but still far from the 0.25% required for AWAKE experiments.

However, it is plausible that the actual density profile in the presented case is closer to the on-axis power profile (figure 13(b)) than to the radially integrated case (figure 13(c)). This highlights the need to develop a 2D-model that can take

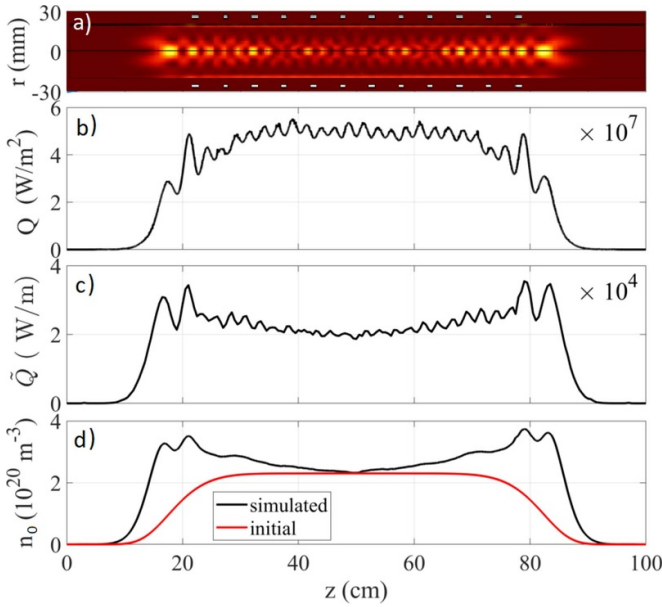


Figure 13. Simulation optimized for homogenous axial density of $2.3 \times 10^{-20} \text{ m}^{-3}$ employs 12 antennas at $p = 8 \text{ Pa}$ Ar, $P = 25 \text{ kW}$ total, and a homogeneous $B_0 = 100 \text{ mT}$. (a) $Q_{\text{wave}}(r, z)$, (b) central lineout $Q_{\text{wave}}(r = 0, z)$, (c) integrated dissipated power $\tilde{Q}(z)$, (d) the initial n_e profile used for the simulation (red) and the resulting density profile n_0 . The electron density variation in the central 0.5 m of the cell is $\pm 10\%$.

into account the full map of the power deposited into the plasma. Furthermore, we find that the power deposition pattern is dominated by the near field of the antennas and that a variation of the initial electron density or the exact antenna spacing can result in strongly varying interference patterns. However, these fluctuations have only a minor influence on the resulting n_e profile, so that an even closer spacing of the antennas is not resulting in a more homogeneous plasma density. The simulations suggest that a setup with an antenna spacing around 5 cm could be suitable to achieve a relatively homogeneous n_e profile in a range of electron density amplitudes. The density tuning could be achieved by the power and DC magnetic field applied to the system.

6. Discussion

We presented here the results of the first TS measurements obtained at the optical view port location of the HPS for the AWAKE experiment. In contrast to previous experiments [28], in the present campaign, the source was operated with ring antennas. The TS diagnostics provides locally and temporally resolved measurements of the electron density and the electron temperature that were compared to a 1D PPM.

Utilizing the purely collisional power dissipation from the helicon wave to the plasma, the plasma parameters measured in the experiment could be reproduced, suggesting that the plasma is sustained fully by collisional power dissipation. The simulation results in a homogeneous T_e profile, promoted by the fast thermalization of electrons. The global electron

temperature is determined by the neutrals density and the plasma geometry. The obtained n_e profiles, in contrast, exhibit a strong inhomogeneity along the axial coordinate. This is due to two factors, the strongly localized power deposition at the antenna locations, that is overestimated in the present radially-integrated 1D model, and the low mobility of the ions, that is likely underestimated by neglecting neutral depletion.

The general trends measured in different operating conditions could be well-reproduced by the model. In particular, we observe a decrease in T_e when the gas pressure increases and when the particle losses increase due to reduced confinement at low magnetic fields. In contrast, T_e is not affected by the power deposited into the plasma. The increased n_e at the view port position with increased magnetic field is caused by the promotion of wave propagation into the inter-antenna gap and reduced losses to the lateral boundary. The measured saturation of the electron density with provided power, however, was not reproduced by the present model due to several physical processes not accounted for.

A considerable improvement of the plasma homogeneity was achieved in the model by improving the homogeneity of the DC magnetic field and by simulating a large number of antennas. With 12 antennas, the simulation predicts an n_e profile with a smooth gradient leading to a density variation of $< 10\%$ over the central 50 cm of the HPS, in contrast to the present $> 50\%$. Moreover, due to the simplifications applied in this 1D model, we expect the real density profile to exhibit an even better homogeneity.

In order to deeper understand the physical phenomena that lead to establishing the steady-state plasma parameter distributions in the HPS, further investigations are required. Future experimental campaigns are planned to extend the power and pressure scans and to obtain detailed radial and axial n_e and T_e profiles. These data will be used to benchmark an improved 2D PPM that will allow to account for the significantly different power deposition profiles along the HPS. Furthermore, introducing the mechanism of neutral depletion will enable us to advance the modeling of the electron density established at high power.

During the present measurement campaign, a maximum electron density of $3 \times 10^{-20} \text{ m}^{-3}$ was measured at the optical view port. This is more than a factor of two lower than the nominal AWAKE density of $7 \times 10^{-20} \text{ m}^{-3}$ which had been measured previously by interferometry [28]. Changing the antennas and other experimental conditions detailed in section 2 (pumping scheme, insulation, grounding, matching), might have impacted the power transfer efficiency in the present setup. In the PPM, such an impaired efficiency could have been compensated by an overestimation of the losses at the plasma surface. Furthermore, significantly different axial density profiles generated by the ring antennas in comparison to the previously employed half-helical antennas might be responsible for the lower measured electron density at the view port. The comparison of the plasma parameters achieved with different types of antennas will be subject to future investigations. Furthermore, the violation of the cylindrical symmetry due to the view port might affect the plasma distribution.

Diffusion of the plasma into the view port probably causes a reduced on-axis density at this location, while an extended plasma width might have caused an overestimation of the central plasma density in the chord-integrated interferometer measurement [28].

The potential effect of the view ports on the plasma symmetry highlights the need to utilize a cylindrically symmetric quartz tube for the HPS. Therefore, we are planning to adjust the collection branch of the TS diagnostic to account for the curvature of the quartz tube. This setup would enable the measurement of axial density profiles along the entire length of the quartz tube, in particular, close to the antenna positions. However, careful mitigation of laser reflections from the wall of the quartz tube has to be implemented, as a black coating, as presently used opposite to the view port, will not be possible in this configuration.

The accuracy of the electron density determination of the present TS setup accounts for $\approx 10\%$. For the AWAKE plasma source, a homogeneity of the electron density along the axis of 0.25% is required. In order to assess n_e at this level of precision, the statistical uncertainties have to be reduced, significantly. This could be achieved by accumulating more laser pulses, with the drawback of increasing the effective integration time. Another strategy to improve the SNR could be to increase the throughput of the optical system. Utilizing a larger width of the spectrometer entrance slit, however, compromises the performance of the notch filter and the precision of the fits for the Thomson spectra and the calibration Raman spectra. A local, on-line diagnostic of the electron density at the precision of 0.25%, therefore, requires further significant development.

7. Conclusions

We report on the first TS measurements in the HPS for AWAKE. The diagnostic provides precise, local, temporally-resolved electron density and temperature data at the optical view port position. The experimental data are compared to a 1D PPM, where the input power is determined from the simulation of the propagation of the helicon wave in the plasma. It was found that a purely collisional power deposition is compatible with the measured plasma parameters. Furthermore, the general trends of the plasma parameters with the variation of the experimental parameters have been reproduced. However, in order to simulate the saturation of the measured electron density with the RF power, the model requires further refinement. The simulation results suggest the presence of strong variations of the electron density along the plasma axis, that are likely overestimated in the simple 1D approach of the present model. Nevertheless, the simulation demonstrates that the plasma homogeneity can be significantly improved by providing a homogeneous DC magnetic field and a large number of antennas, approximately one antenna every five centimeters. The highest electron densities measured in the present configuration with ring-antennas were $3 \times 10^{-20} \text{ m}^{-3}$, about a factor of 2.5 smaller than required for optimum conditions in electron acceleration experiments at AWAKE. The

effect of the utilized antenna type on the achievable electron density is subject to future research. Additionally, extending the measurements to cover a larger pressure and power range and to obtain radial and axial plasma profiles is planned. An improved 2D PPM, including additional effects such as neutrals depletion, is currently under development and will be validated with the available experimental data. Additional simulations will be guiding the development of an updated 2.5 m HPS prototype that should meet the design requirements for the future modular AWAKE *accelerator*. Furthermore, the TS diagnostic is planned to be employed to characterize the n_e homogeneity of AWAKE's DPS. By providing reliable plasma parameters across different plasma sources, the developed TS setup is expected to contribute significantly to the AWAKE project and to the advancement of the simulation of helicon plasma sources.

Data availability statement

The data cannot be made publicly available upon publication because they are not available in a format that is sufficiently accessible or reusable by other researchers. The data that support the findings of this study are available upon reasonable request from the authors.

Acknowledgments

The authors thank P Muggli for valuable discussions. This work was partially supported by the Swiss National Fund Grant No 200020-204983.

ORCID iDs

C Stollberg  <https://orcid.org/0000-0001-6102-0898>
 Ph Guittienne  <https://orcid.org/0009-0003-7272-6505>
 R Karimov  <https://orcid.org/0009-0003-5047-2516>
 A Sublet  <https://orcid.org/0000-0002-3165-7449>
 I Furno  <https://orcid.org/0000-0001-8348-1716>
 B Vincent  <https://orcid.org/0000-0001-5420-6002>
 B Buttenschön  <https://orcid.org/0000-0002-9830-9641>

References

- [1] Tajima T and Dawson J M 1979 Laser electron accelerator *Phys. Rev. Lett.* **43** 267–70
- [2] Gschwendtner E and Muggli P 2019 Plasma wakefield accelerators *Nat. Rev. Phys.* **1** 246–8
- [3] Esarey E, Schroeder C B and Leemans W P 2009 Physics of laser-driven plasma-based electron accelerators *Rev. Mod. Phys.* **81** 1229–85
- [4] Adli E *et al* 2018 Acceleration of electrons in the plasma wakefield of a proton bunch *Nature* **561** 363–7
- [5] Gschwendtner E *et al* 2022 The awake run 2 programme and beyond *Symmetry* **14** 1680
- [6] Adli E *et al* 2019 Experimental observation of proton bunch modulation in a plasma at varying plasma densities *Phys. Rev. Lett.* **122** 054802

- [7] Verra L *et al* 2023 Development of the self-modulation instability of a relativistic proton bunch in plasma *Phys. Plasmas* **30** 083104
- [8] Braunmüller F *et al* 2020 Proton bunch self-modulation in plasma with density gradient *Phys. Rev. Lett.* **125** 264801
- [9] Plyushchev G, Kersevan R, Petrenko A and Muggli P 2017 A rubidium vapor source for a plasma source for awake *J. Phys. D: Appl. Phys.* **51** 025203
- [10] Öz E and Muggli P 2014 A novel Rb vapor plasma source for plasma wakefield accelerators *Nucl. Instrum. Methods Phys. Res. A* **740** 197–202
- [11] Torrado N E, Lopes N C, Silva J F A, Amoedo C and Sublet A 2023 Double pulse generator for unipolar discharges in long plasma tubes for the awake experiment *IEEE Trans. Plasma Sci.* **51** 3619–27
- [12] Verra L *et al* 2024 Filamentation of a relativistic proton bunch in plasma *Phys. Rev. E* **109** 055203
- [13] Turner M *et al* 2024 Experimental Observation of Motion of Ions in a Resonantly Driven Plasma Wakefield Accelerator (arXiv: 2406.16361)
- [14] Amoedo C *et al* 2025 Demonstration of proton bunch self-modulation in a discharge plasma source (in preparation)
- [15] Isayama S, Shinohara S and Hada T 2018 Review of helicon high-density plasma: production mechanism and plasma/wave characteristics *Plasma Fusion Res.* **13** 1101014–1101014
- [16] Goulding R H *et al* 2017 Progress in the development of a high power helicon plasma source for the materials plasma exposure experiment *Fusion Sci. Technol.* **72** 588–94
- [17] Thakur S C, Simmonds M J, Caneses J F, Chang F, Hollmann E M, Doerner R P, Goulding R, Lumsdaine A, Rapp J and Tynan G R 2021 Pisces-rf: a liquid-cooled high-power steady-state helicon plasma device *Plasma Sources Sci. Technol.* **30** 055014
- [18] Van Compernelle B *et al* 2021 The high-power helicon program at DIII-D: gearing up for first experiments *Nucl. Fusion* **61** 116034
- [19] Furno I, Agnello R, Fantz U, Howling A, Jacquier R, Marini C, Plyushchev G, Guittienne P and Simonin A 2017 Helicon wave-generated plasmas for negative ion beams for fusion 22 *Topical Conf. on Radio-Frequency Power in Plasmas* (<https://doi.org/10.1051/epjconf/201715703014>)
- [20] Jacquier R *et al* 2023 A double-ended helicon source to symmetrize raid plasma *Fusion Eng. Des.* **192** 113614
- [21] Chang Díaz F R, Giambusso M, Corrigan A M H, Dean L O and Warrayat M F 2022 Recent progress on the vasmr engine 37th *Int. Electric Propulsion Conference/Massachusetts Institute of Technology* (Ad Astra Rocket Company) p 77598
- [22] Ziembra T, Euripides P, Slough J, Winglee R, Giersch L, Carscadden J, Schnackenberg T and Isley S 2006 Plasma characteristics of a high power helicon discharge *Plasma Sources Sci. Technol.* **15** 517
- [23] Green J and Schmitz O 2020 Construction of a linear plasma device for studying helicon plasmas relevant to plasma-wakefield accelerators *Plasma Sources Sci. Technol.* **29** 045008
- [24] Green J, Schmitz O and Zepp M 2020 Direct measurement of the ionization source rate and closure of the particle balance in a helicon plasma using laser induced fluorescence *Phys. Plasmas* **27** 043511
- [25] Granetzny M, Dwinell J, Elward B, Rakers K, Zepp M and Schmitz O 2020 Helicon wave modelling for the madison awake prototype map 62nd *Annual Meeting of the APS Division of Plasma Physics*
- [26] Granetzny M, Schmitz O and Zepp M 2023 Preference of right-handed whistler modes and helicon discharge directionality due to plasma density gradients *Phys. Plasmas* **30** 120701
- [27] Agnello R, Andrebe Y, Arnichand H, Blanchard P, De Kerchove T, Furno I, Howling A A, Jacquier R and Sublet A 2020 Application of thomson scattering to helicon plasma sources *J. Plasma Phys.* **86** 905860306
- [28] Buttenschön B, Fahrenkamp N and Grulke O 2018 A high power, high density helicon discharge for the plasma wakefield accelerator experiment AWAKE *Plasma Phys. Control. Fusion* **60** 075005
- [29] Lechte C, Stöber J and Stroth U 2002 Plasma parameter limits of magnetically confined low temperature plasmas from a combined particle and power balance *Phys. Plasmas* **9** 2839–46
- [30] Vincent B 2019 Incoherent Thomson scattering investigations in Hall thruster, planar magnetron and ECR ion source plasmas *PhD Thesis* Universite d'orleans
- [31] Glebov A L, Mokhun O, Rapaport A, Vergnole S, Smirnov V and Glebov L B 2012 Volume Bragg gratings as ultra-narrow and multiband optical filters *Proc. SPIE* **8428** 84280C
- [32] Vincent B, Tsikata S, Mazouffre S, Minea T and Fils Jôme 2018 A compact new incoherent thomson scattering diagnostic for low-temperature plasma studies *Plasma Sources Sci. Technol.* **27** 055002
- [33] Penney C M, St. Peters R L and Lapp M 1974 Absolute rotational Raman cross sections for n_2 , o_2 and co_2 *J. Opt. Soc. Am.* **64** 712–6
- [34] Lieberman M A and Lichtenberg A J 2005 *Principles of Plasma Discharges and Materials Processing* (Wiley)
- [35] Klozenberg J P, McNamara B and Thonemann P C 1965 The dispersion and attenuation of helicon waves in a uniform cylindrical plasma *J. Fluid Mech.* **21** 545–63
- [36] Guittienne P, Jacquier R, Pouradier Duteil B, Howling A A, Agnello R and Furno I 2021 Helicon wave plasma generated by a resonant birdcage antenna: magnetic field measurements and analysis in the RAID linear device *Plasma Sources Sci. Technol.* **30** 075023
- [37] Fruchtman A, Makrinich G, Chabert P and Rax J M 2005 Enhanced plasma transport due to neutral depletion *Phys. Rev. Lett.* **95** 115002
- [38] Comsol inc 2021 multiphysics software from comsol (available at: www.comsol.com)
- [39] Guittienne P, Howling A A and Furno I 2024 *Resonant Network Antennas for Radio-Frequency Plasma Sources: Theory, Technology and Applications* (Institute of Physics Publishing)
- [40] Guittienne P, Howling A A and Furno I 2018 Two-fluid solutions for Langmuir probes in collisionless and isothermal plasma, over all space and bias potential *Phys. Plasmas* **25** 093519
- [41] Chen F F 1991 Plasma ionization by helicon waves *Plasma Phys. Control. Fusion* **33** 339
- [42] Chen F F and Blackwell D D 1999 Upper limit to landau damping in helicon discharges *Phys. Rev. Lett.* **82** 2677–80
- [43] Degeling A W and Boswell R W 1997 Modeling ionization by helicon waves *Phys. Plasmas* **4** 2748–55
- [44] Hagelaar G J M and Pitchford L C 2005 Solving the boltzmann equation to obtain electron transport coefficients and rate coefficients for fluid models *Plasma Sources Sci. Technol.* **14** 722
- [45] Zel'dovich Y B and Raizer Y B 1967 *Physics of Shock Waves and High-Temperature Hydrodynamic Phenomena* (Dover Books on Physics. Elsevier Inc.,)
- [46] Baalrud S D, Scheiner B, Yee B, Hopkins M and Barnat E 2015 Extensions and applications of the bohm criterion *Plasma Phys. Control. Fusion* **57** 044003